European Journal of Mechanics / A Solids 96 (2022) 104756

Contents lists available at ScienceDirect

European Journal of Mechanics / A Solids

journal homepage: www.elsevier.com/locate/ejmsol

Are the terms *stiffening/softening structures* mechanically unambiguous?

Johannes Kalliauer *, Herbert A. Mang

Institute for Mechanics of Materials and Structures, Technische Universität Wien – TU Wien, Karlsplatz 13/202, 1040 Vienna, Austria

ARTICLE INFO

Keywords:
Stiffening/softening structure
Stiffness measurement
Finite element method
Linear elasticity
Stability
Structures

ABSTRACT

The purpose of this paper is to give a conditionally affirmative answer to the question posed in its title. The tool that enables such an answer is a mechanically objective arc-length in the form of a representative displacement of the structure. In this context, mechanical objectivity is defined as the independence of model parameters, such as the chosen finite element or the discretization of the investigated structure in the framework of a consistent mesh refinement. It guarantees, *e.g.*, the mechanical objectivity of the transition from a stiffening to a softening structure and *vice versa*. It is shown numerically that at this point some characteristic degrees of freedom (d.o.f.) of the investigated structure are stiffening while others are softening. Hence, individual d.o.f. are, in general, unsuitable for marking extreme values of the stiffness of structures. A global quantity, alternative to the suggested stiffness in this work, is the extreme value of the determinant of the tangent stiffness matrix. It is shown numerically that, in general, this value depends on arbitrary model parameters and, therefore, does not have a physical meaning. An oblate rotational ellipsoidal shell, subjected to internal pressure, serves as an example for buckling of a stiffening shell, contradicting the widespread misconception of buckling being restricted to non-stiffening structures.

1. Introduction

If, at a particular load intensity of proportional loading, the stiffness of a structure is increasing, it will be termed herein a *stiffening structure*. This term, however, must not be confused with the one of *stiffening of a structure*, expressing a modification of its design rather than a continuous change of the mechanical state of a proportionally loaded structure. In mechanics of materials, *softening* denotes, in a factually as well as linguistically unambiguous manner, the antonym of *hardening*. In structural mechanics, however, there seems to be no generally accepted expression of the opposite of the term *stiffening*. This might be the reason why this term was occasionally combined with the term *hardening/softening* to *stiffness hardening/softening* (Kim and Song, 2016; Wang et al., 2018). For convenience, the expressions *hardening/softening of structures* were sometimes used as pseudo-synonyma of the linguistically more ponderous mechanical terms *increasing/decreasing stiffness of structures* (Kanodia et al., 1977; Mang and Jia, 2013). In this work, *softening* will be used as the antonym of *stiffening*. Whether or not the terms *stiffening/softening structures*, in the aforementioned sense, are mechanically unambiguous, depends on their definitions. Usually, a proportionally loaded structure is termed stiffening (softening) at a specific load level if $\mathrm{d}^2\lambda/\mathrm{d}q_i^2 > 0$ (< 0), assuming $\mathrm{d}\lambda/\mathrm{d}q_i > 0$, with $\mathrm{d}\lambda > 0$ and $\mathrm{d}q_i > 0$. In the framework of the Finite Element Method (FEM), λ is a dimensionless proportionality factor by which the vector of reference node forces, $\bar{\mathbf{P}}$, is multiplied; q_i denotes a characteristic degree of freedom (d.o.f.). The problem with these definitions of proportionally loaded stiffening/softening structures is their local, *i.e.* d.o.f.-related character. In general, a specific load level at which $\mathrm{d}^2\lambda/\mathrm{d}q_i^2 = 0$ does not mean a transition from stiffening (softening) to softening (stiffening) of the structure, because the point of inflection of the $\lambda - q_i$ diagram is merely a local feature.

Therefore, the search for a mechanically objective criterion for *stiffening/softening* structures must be directed to finding a global mechanical quantity which defines these terms unambiguously. Herein, two quantities will be checked for their ability to mark, in a mechanically objective manner, the transition from stiffening (softening) to softening (stiffening). These quantities are (i) extreme values of the normalized determinant of the tangent stiffness matrix $\mathbf{K}_T$ and (ii) points of inflection of a function $\xi(\lambda)$, where ξ represents a special form of an arc length. In this context, mechanical objectivity means that the load-level for which $\mathrm{d}(\det \mathbf{K}_T)/\mathrm{d}\lambda = 0$ and $\mathrm{d}^2\lambda/\mathrm{d}\xi^2 = 0$, is independent of (i) the chosen finite element and (ii) the number of finite elements in the framework of a consistent refinement of the mesh. The reason for the restriction of the numerical investigation to the linear elastic material domain is to show that extreme values of the stiffness of proportionally loaded structures may even occur for constant material stiffness. In other words, we want to avoid a possible confusion of

* Corresponding author.
E-mail addresses: johannes.kalliauer@tuwien.ac.at (J. Kalliauer), Herbert.Mang@tuwien.ac.at (H.A. Mang).

https://doi.org/10.1016/j.euromechsol.2022.104756
Received 2 March 2022; Received in revised form 6 July 2022; Accepted 28 July 2022
Available online 6 August 2022

the terms “stiffening structures” and “hardening materials”. However, the methods, investigated in this work for their ability to determine extreme values of the stiffness of proportionally loaded structures, are not restricted to linear elasticity.

Apart from scientific curiosity it is deemed useful to know whether or not the investigated structure is stiffening at least in a sufficiently large initial range of the proportionality factor λ. By this range of λ we mean the prebuckling domain, assuming that a stability limit exists. Stiffening, in the previously defined sense, precludes snap-through of the perfect structure. However, it does not preclude bifurcation buckling with a potentially dangerous postbuckling behavior. Although we will touch on this topic at the end of the numerical investigation, the focus of our work is on the terms *stiffening/softening* in the prebuckling regime.

The remaining part of the paper consists of three sections. Section 2 deals with the two aforementioned global quantities that will be checked for their ability to mark the transition from a stiffening to a softening structure and *vice versa*. Conversely, these quantities will also be checked for maintaining their signs in case of no such transitions. Section 3 is devoted to a comprehensive numerical investigation of structures subjected to monotonically increasing quasi-static loads. In the first two examples, linear elastic bars will be considered. The reason for the restriction to such simple structures is to emphasize the significance of the terms *stiffening/softening structures* in this work as opposed to the meaning of *hardening* and *softening of materials*. The first example is characterized by two stability limits, $\lambda_{S^+} > 0$ and $\lambda_{S^-} < 0$. Since $\mathbf{K}_T$ is positive definite in the open interval $(\lambda_{S^-}, \lambda_{S^+})$, $\det \mathbf{K}_T > 0$ in this interval. Consequently, $\det \mathbf{K}_T(\lambda)$ must have a maximum value located between λ_{S^-} and λ_{S^+}. The characteristic features of the second example are the absence of a stability limit, but the existence of a transition from softening to stiffening of the structure. This example is also used for computation of the mean displacement of the bar, u_{ave}, for a particular load intensity. This quantity is related to the aforementioned parameter ξ. The purpose of this analysis is the investigation of the rates of convergence of u_{ave} for uniform as well as non-uniform meshes. The third example deals with buckling of a stiffening structure of the form of an oblate rotational ellipsoidal shell, subjected to internal pressure. The $\lambda - u_{ave}$ diagram is used to explain the initial postbuckling behavior of the perfect structure. Section 4 contains the conclusions drawn from this work.

2. Global quantities to be checked for their ability to identify *stiffening/softening structures*

2.1. $\mathrm{d}(det\ \mathbf{K}_T)/\mathrm{d}\lambda$

The historical background of this quantity is a paper on buckling of a cylindrical pressure vessel with a torispherical head (Kanodia et al., 1977; Mang and Jia, 2013), see Fig. 1(a). Obviously, such a structure may buckle under external pressure. However, it may also buckle under internal pressure which produces circumferential compressive stresses in the toroidal knuckle of containers with shallow torispherical closures (Adachi and Benicek, 1964; Galletly, 1982; Helnwein, 1996; Mang and Jia, 2013). Fig. 1(b) shows a schematic $\det \mathbf{K}_T / \det(\mathbf{K}_T)_0 - \lambda$ diagram, in distorted scale, where $(\mathbf{K}_T)_0$ denotes the tangent stiffness matrix at the onset of loading, see point A(0,1). This diagram has a maximum value at point M, *i.e.* at a load level in the open interval between the two stability limits λ_{S^-} and λ_{S^+}.

This has prompted the authors of Kanodia et al. (1977) and Mang and Jia (2013) to interpret the part $\widehat{AM}$ of the $\det \mathbf{K}_T / \det(\mathbf{K}_T)_0 - \lambda$ diagram, see Fig. 1(b), as an indicator of “the initial load-hardening nature of the structure” if subjected to internal pressure. (Consistent with this interpretation is the one of part $\widehat{AS^-}$ of the $\det \mathbf{K}_T / \det(\mathbf{K}_T)_0 - \lambda$ diagram in Fig. 1(b) as an indicator of a softening structure if subjected to external pressure.) Based on the mechanical interpretation of part $\widehat{AM}$ of the said diagram, it did not seem unreasonable to regard point M as marking the transition from a stiffening to a softening structure. However, this is in conflict with a $\lambda - q_i$ diagram in Kanodia et al. (1977), where q_i denotes a characteristic d.o.f. of the toroidal knuckle. Fig. 2 contains a qualitative reproduction of Fig. 11 in Kanodia et al. (1977). It shows a part of the primary and of the corresponding secondary load–displacement path. The strictly positive curvatures of the two curves in this diagram create the impression of continuous stiffening of the structure, notwithstanding the problematic nature of classifying a structure as stiffening at the considered load level on the basis of a single degree of freedom. The authors of Mang and Jia (2013) went even further in the conclusions of their work, stating that “the physical meaning of a maximum of the determinant of the tangent stiffness matrix in the prebuckling regime is the one of a minimum of the percentage bending energy of the total strain energy”.

2.2. $\mathrm{d}^2\lambda/\mathrm{d}\xi^2$

In the framework of the FEM, the differential form of the equilibrium equations is given as

$$\mathbf{K}_T \cdot \mathrm{d}\mathbf{q} = \mathrm{d}\lambda\, \bar{\mathbf{P}}\,. \tag{1}$$

Division of (1) by a differential of the arc-length ξ yields

$$\mathbf{K}_T \cdot \frac{\mathrm{d}\mathbf{q}}{\mathrm{d}\xi} = \frac{\mathrm{d}\lambda}{\mathrm{d}\xi}\, \bar{\mathbf{P}}\,. \tag{2}$$

ξ is a dimensionless quantity. For one-dimensional structures, it is defined herein as

$$\xi = \frac{u_{\mathrm{ave}}}{\int \mathrm{d}s}\,, \tag{3}$$

where

$$u_{\mathrm{ave}} = \frac{\int \|\mathbf{u}\|\, \mathrm{d}s}{\int \mathrm{d}s}\,, \tag{4}$$

with $\mathbf{u}$ standing for the displacement vector; $\mathrm{d}s$ denotes the length of the axis of an infinitesimal element of a structural member. Thus, u_{ave} represents the mean displacement of the structure. (3) holds for a system with an infinite number of degrees of freedom. In FE analysis, the integrals in (3) and (4) are to be replaced by sums of integrals stretching over the individual finite elements. Accordingly, in these integrals $\mathbf{u}$ is to be understood as an element-related, *i.e.* a local quantity. It is obtained by means of interpolation between nodal displacements. For two-dimensional structures, $\mathrm{d}s$ in (4) is to be replaced by $\mathrm{d}A$, denoting the area of an infinitesimal element of the midsurface of a structural member. $\int \mathrm{d}s$ in Eq. (3) should be replaced by $\sqrt{\int \mathrm{d}A}$. The advantage of the proposed arc-length ξ over its standard form, commonly defined as $\xi^* = \|\mathbf{q}\|$ (Helnwein and Mang, 1997; Mang et al., 2016; Mang, 2017), is its independence of (i) the chosen type of finite element (displacement-based or hybrid), (ii) the number of node points, (iii) the mode of mesh refinement, and (iv) the chosen unit of length, noting that $\xi^* = \|\mathbf{q}\|$ would not be independent of it if $\mathbf{q}$ contained components with different dimensions. Differentiation of (2) with respect to ξ results in

$$\frac{\mathrm{d}\mathbf{K}_T}{\mathrm{d}\xi} \cdot \frac{\mathrm{d}\mathbf{q}}{d\xi} + \mathbf{K}_T \cdot \frac{\mathrm{d}^2\mathbf{q}}{\mathrm{d}\xi^2} = \frac{\mathrm{d}^2\lambda}{\mathrm{d}\xi^2}\, \bar{\mathbf{P}}\,. \tag{5}$$

In the prebuckling regime, the stiffness of elastic structures is positive. Thus, for $\xi \geq 0$, with $\lambda = 0 \Leftrightarrow \xi = 0$,

$$0 < \mathrm{sgn}(\lambda)\, \frac{\mathrm{d}\lambda}{\mathrm{d}\xi} < \infty \quad \Leftrightarrow \quad 0 < \frac{\mathrm{d}|\lambda|}{\mathrm{d}\xi} < \infty\,, \tag{6}$$

with sgn denoting the sign function (Denman and Beavers, 1976; Kenney and Laub, 1995).

Stiffening (softening) structures are characterized by

$$\frac{\mathrm{d}^2|\lambda|}{\mathrm{d}\xi^2} > 0\ (< 0)\,. \tag{7}$$

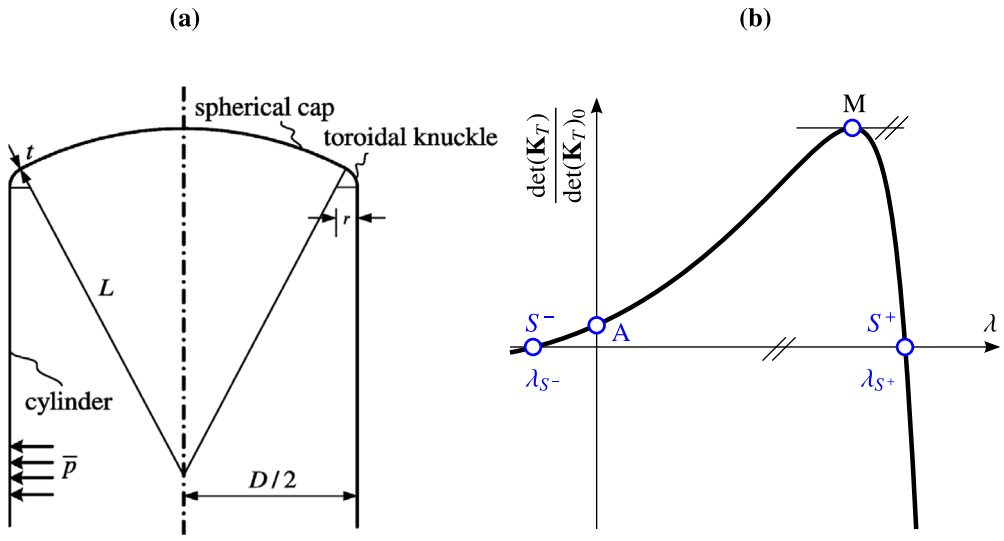

Fig. 1. Cylindrical pressure vessel with a torispherical head: (a) axial section of a part of the structure, taken from Mang and Jia (2013), (b) schematic $\det(\mathbf{K}_T)/\det(\mathbf{K}_T)_0 - \lambda$ diagram (λ_{S^-}: stability limit for external pressure, λ_{S^+}: stability limit for internal pressure), in distorted scale, based on Figs. 9 and 10 in Kanodia et al. (1977).

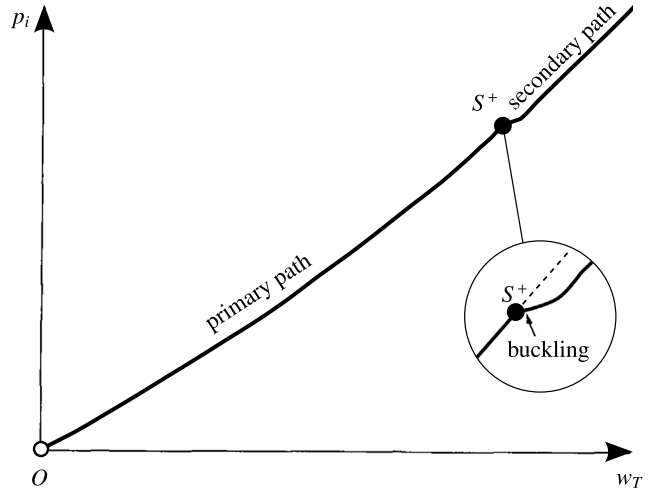

Fig. 2. Part $\widehat{OS^+}$ of a sketch of a $p_i - w_T$ diagram of a point of the toroidal knuckle, continued by a stretch of the corresponding postbuckling path (p_i ... internal pressure, w_T ... transverse displacement), based on Fig. 11 in Kanodia et al. (1977). For the sake of better visualization, the distance of the secondary part from the primary path, indicated in the detail of this figure, was enlarged.

Following from (5), the conditions for the transition from stiffening (softening) to softening (stiffening) are obtained as

$$\frac{\mathrm{d}^2\lambda}{\mathrm{d}\xi^2} = 0\,, \qquad \frac{\mathrm{d}\mathbf{K}_T}{\mathrm{d}\xi}\cdot\frac{\mathrm{d}\mathbf{q}}{\mathrm{d}\xi} + \mathbf{K}_T\cdot\frac{\mathrm{d}^2\mathbf{q}}{\mathrm{d}\xi^2} = \mathbf{0}\,. \tag{8}$$

At $\lambda = 0$,

$$\lim_{h\searrow 0}\frac{\mathrm{d}\lambda}{\mathrm{d}\xi}(\lambda = h) = -\lim_{h\nearrow 0}\frac{\mathrm{d}\lambda}{\mathrm{d}\xi}(\lambda = h) \tag{9}$$

and

$$\lim_{h\searrow 0}\frac{\mathrm{d}^2\lambda}{\mathrm{d}\xi^2}(\lambda = h) = \lim_{h\nearrow 0}\frac{\mathrm{d}^2\lambda}{\mathrm{d}\xi^2}(\lambda = h) = \lim_{h\to 0}\frac{\mathrm{d}^2\lambda}{\mathrm{d}\xi^2}(\lambda = h)\,, \tag{10}$$

where $\lim_{h\searrow h_i} f(h)$, $\lim_{h\nearrow h_i} f(h)$, and $\lim_{h\to h_i} f(h)$ denote the left-sided, the right-sided, and the two-sided limit at $h = h_i$, respectively.

Table 1
Details of the Abaqus elements B21 and B22 (Abaqus User Manual, 2020).

Designation	Formulation	# of nodes	# of d.o.f.
Abaqus B21	2D, displ., Timoshenko	2/linear	$6(=2\cdot 3)$
Abaqus B22	2D, displ., Timoshenko	3/quad.	$9(=3\cdot 3)$

3. Numerical investigation

3.1. IPE 400 bar subjected to a centric axial force at its midpoint

3.1.1. Preliminaries

Fig. 3(a) shows the structure. The length of the bar is $2L$, with $L = 5\,\mathrm{m}$. Its cross-section is shown in Fig. 3(b). The area of the cross-section, A, is equal to $8.0678\ 10^{-3}\,\mathrm{m}^2$. Its second moment of inertia about the y-axis, I_y, is equal to $2.18765\ 10^{-4}\,\mathrm{m}^4$. The modulus of elasticity, E, and Poisson's ratio, ν, are equal to $2.1\ 10^{11}\,\mathrm{N/m}^2$ and 0.3, respectively. At its two end points, the bar is simply supported. Its midpoint can only move in the axial direction. At this point, the bar is subjected to a centric axial force $P = \lambda\,\bar{P}$, with $\bar{P} = 6.6545\ 10^7\,\mathrm{N}$ as the reference load. The load is applied quasi-statically.

The numerical investigation was carried out with the help of the commercial software Abaqus (Abaqus User Manual, 2020), using SI units, *i.e.* "m" and "kg/s^2". Details of the Abaqus elements B21 and B22, employed in the analysis, are given in Table 1.

3.1.2. Numerical results

Discretization error at the stability limits. For $P \geq 0\ (\leq 0)$, $\lambda = P/\bar{P} \geq 0\ (\leq 0)$. Thus, depending on the direction of P, the stability limit $P_S = \lambda_S\,\bar{P}$ is either a positive or a negative quantity. In other words, the structure has two stability limits. At $\lambda = \lambda_{S^+} > 0$, the upper span of the bar starts buckling. At $\lambda = \lambda_{S^-} = -\lambda_{S^+} < 0$, the lower span of the bar starts buckling. To check the discretization error of the bar at λ_{S^+} and λ_{S^-}, respectively, the following linear eigenvalue problem, proposed by the second author (Malendowski) in Kalliauer et al. (2021), was solved:

$$\left[\mathbf{K}_T - \chi_i\,(\mathbf{K}_T)_0\right]\cdot\mathbf{r}_i = \mathbf{0}, \quad i = 1, 2, \ldots, N. \tag{11}$$

In (11), χ_i and $\mathbf{r}_i$ denote the ith eigenvalue and the corresponding eigenvector, respectively, whereas N stands for the number of d.o.f. of the bar, subdivided into finite elements. An advantage of this linear eigenvalue problem over the standard linear eigenvalue problem, with the unit matrix instead of $(\mathbf{K_T})_0$ in (11), is its consistency regarding units and the automatic normalization of $(\chi_i)_0 := \chi_i(\lambda = 0)$ to 1.

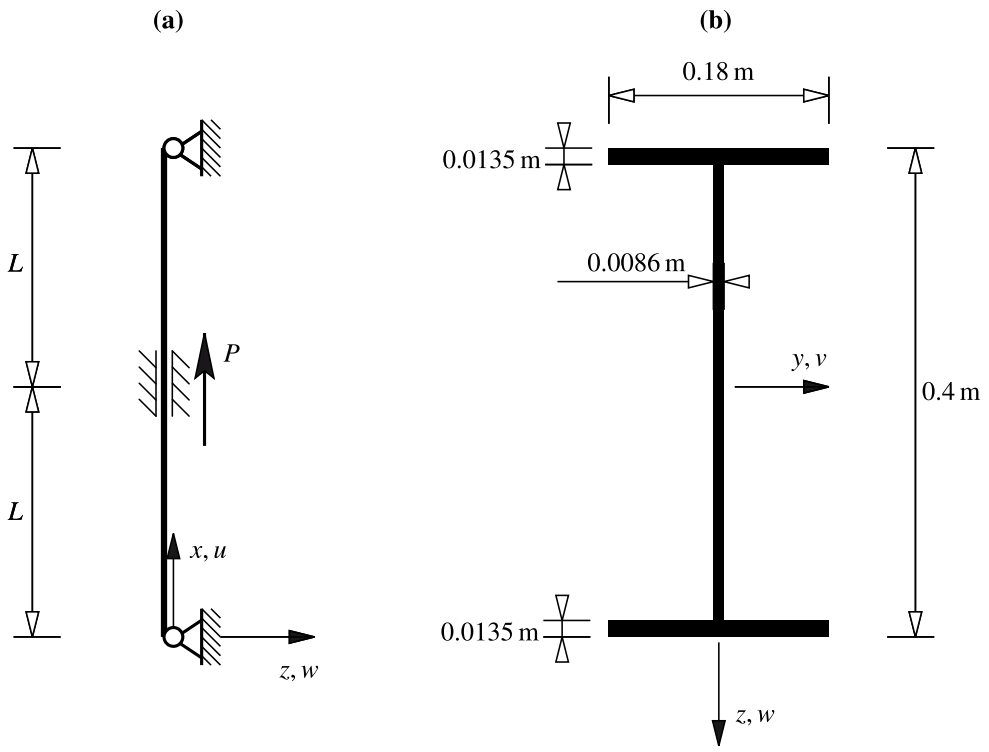

Fig. 3. Bar subjected to a centric axial force at its midpoint: (a) structure, (b) cross-section.

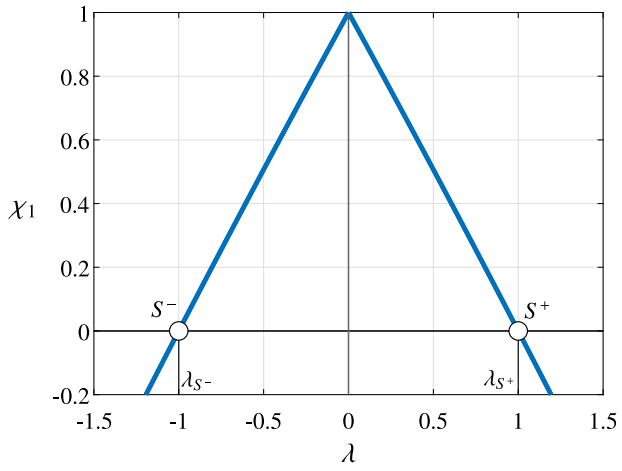

Fig. 4. Bar subjected to a centric axial force at its midpoint: $\chi_1 - \lambda$ diagram obtained with 256 Abaqus elements B22 of equal length in each one of the two spans.

The convergence study for determination of the discretization error at the stability limits was performed with 2, 4, 8, 16, 32, 64, 128, and 256 Abaqus elements B22 of equal length in each one of the two spans of the bar. For four elements in each span the discretization error was less than 0.4%, considering the deviation of the numerical result for $\lambda_{S^+} = -\lambda_{S^-}$, obtained with 256 elements, from the solutions with finer meshes as negligibly small.

Fig. 4 shows the $\chi_1 - \lambda$ diagram obtained with 256 Abaqus elements B22 in each one of the two spans. It is symmetric with respect to $\lambda = 0$. Setting the reference load $\bar{P}$ equal to $|P_S| = 6.6545\ 10^7$ N, yields $\lambda_{S^+} = -\lambda_{S^-} = 1$. The convergence study was repeated with Abaqus elements B21. The differences of the results obtained by the two different finite elements are negligible.

det $\mathbf{K_T}/\max(det\ \mathbf{K_T}) - \lambda$ *diagrams.* Premultiplication of (11) by $(\mathbf{K}_T)_0^{-1}$ gives

$$\left[(\mathbf{K}_T)_0^{-1} \cdot \mathbf{K}_T - \chi_i\, \mathbf{I}\right] \cdot \mathbf{r}_i = \mathbf{0}, \qquad i = 1, 2, \dots, N\,, \tag{12}$$

where $\mathbf{I}$ denotes the unit matrix. Following from the characteristic equation of the determinant of the coefficienct matrix in Eq. (12),

$$\det\left[(\mathbf{K}_T)_0^{-1} \cdot \mathbf{K}_T\right] = \prod_{i=1}^{N} \chi_i\,, \tag{13}$$

where, making use of the *Cauchy–Binet* formula,

$$\det\left[(\mathbf{K}_T)_0^{-1} \cdot \mathbf{K}_T\right] = \left[\det(\mathbf{K}_T)_0^{-1}\right] \cdot \left[\det \mathbf{K}_T\right]\,, \tag{14}$$

see, *e.g.* Mehta (2004) and Forrester (2018). Thus,

$$\det \mathbf{K}_T = \frac{\prod_{i=1}^{N} \chi_i}{\det(\mathbf{K}_T)_0^{-1}}\,. \tag{15}$$

Specialization of (15) for $\lambda = 0$, with

$$(\chi_i)_0 := \chi_i(\lambda = 0) = 1, \qquad i = 1, 2, \dots, N\,, \tag{16}$$

following from specialization of (11) for $\lambda = 0$, gives (Bourbaki, 1998)

$$\det(\mathbf{K}_T)_0 = \frac{1}{\det(\mathbf{K}_T)_0^{-1}}\,. \tag{17}$$

Substitution of (17) into (15) results in

$$\det \mathbf{K}_T = \det(\mathbf{K}_T)_0 \prod_{i=1}^{N} \chi_i\,. \tag{18}$$

Fig. 5 shows $\det \mathbf{K}_T/\max(\det \mathbf{K}_T) - \lambda$ diagrams, obtained with 8, 32, and 128 finite elements of equal length in each one of the two spans of the bar. Since the discretizations of the two spans of the bar are identical, the curves in Fig. 5 are symmetric with respect to $\lambda = 0$. Thus, noting that $\det \mathbf{K}_T > 0$ in the prebuckling region,

$$\max(\det \mathbf{K}_T) = \det(\mathbf{K}_T)_0\,. \tag{19}$$

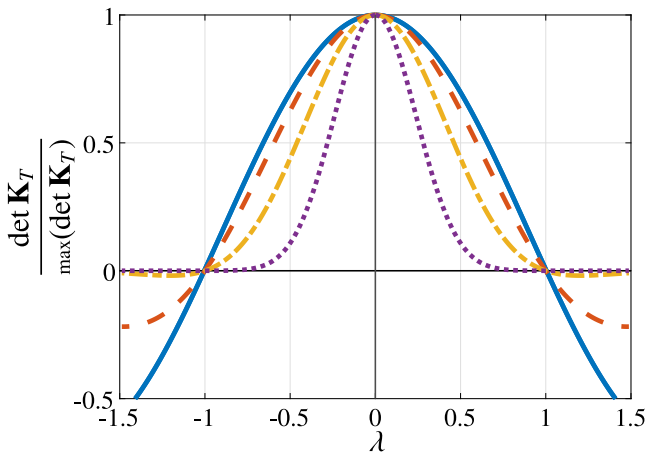

Fig. 5. $\det \mathbf{K}_T/\max(\det \mathbf{K}_T) - \lambda$ diagrams obtained with 4 Abaqus elements B22 (solid blue curve), 16 elements (dashed red curve), 64 elements (dash-dotted yellow curve), and 256 elements (dotted purple curve) in each one of the two spans of the bar. (For interpretation of the references to color in this figure legend, the reader is referred to the web version of this article.)

Following from (18) and (19),

$$\frac{\det \mathbf{K}_T}{\max(\det \mathbf{K}_T)} = \prod_{i=1}^{N} \chi_i \,. \tag{20}$$

With the exception of $\lambda = 0$, $\lambda = \lambda_{S^+}$ and $\lambda = \lambda_{S^-} = -\lambda_{S^+}$, $\prod_{i=1}^{N} \chi_i(\lambda)$ depends on N. Hence, with the exception of these three values of λ, $\det \mathbf{K}_T/\max(\det \mathbf{K}_T)$ depends on N. Fig. 5 shows that, for an arbitrary value of λ, this ratio decreases with increasing N. It is concluded that, for the chosen special discretizations of the bar, the position of $\max(\det \mathbf{K}_T)$ is mesh-independent.

Alternatively, the lower span of the beam was subdivided into twice as many finite elements of equal length as the upper span. Fig. 6(b)–(c) show consistent refinements of the coarsest discretization of the bar, illustrated in Fig. 6(a). Division of (18) by $\max(\det \mathbf{K}_T)$ gives

$$\frac{\det \mathbf{K}_T}{\max(\det \mathbf{K}_T)} = \frac{\det(\mathbf{K}_T)_0}{\max(\det \mathbf{K}_T)} \prod_{i=1}^{N} \chi_i \,. \tag{21}$$

Fig. 7 shows $\det \mathbf{K}_T/\max(\det \mathbf{K}_T) - \lambda$ diagrams obtained with the three discretizations of the bar, shown in Fig. 6. According to Fig. 7, for $\lambda = 0$, where

$$\prod_{i=1}^{N} (\chi_i)_0 = 1 \,, \tag{22}$$

$$\frac{\det(\mathbf{K}_T)_0}{\max(\det \mathbf{K}_T)} < 1 \,. \tag{23}$$

Hence, in contrast to the situation illustrated in Fig. 5, $\det(\mathbf{K}_T)_0$ is not the maximum value of $\det \mathbf{K}_T$ in the prebuckling region. Fig. 7 shows that the value of λ at which $\det \mathbf{K}_T$ becomes a maximum value depends on N. In particular, it elucidates that, for the chosen refinement of the mesh, the values of λ at which $\det \mathbf{K}_T$ becomes a maximum are increasing with growing values of N. Following from Fig. 7,

$$\begin{aligned} \frac{\mathrm{d}(\det \mathbf{K}_T)}{\mathrm{d}\lambda}\bigg|_{\lambda=0} &= \det(\mathbf{K}_T)_0 \sum_{i=1}^{N} \left(\frac{\mathrm{d}\chi_i}{\mathrm{d}\lambda} \prod_{\substack{j=1 \\ j\neq i}}^{N} \chi_j \right)\bigg|_{\lambda=0} \\ &= \det(\mathbf{K}_T)_0 \sum_{i=1}^{N} \frac{\mathrm{d}\chi_i}{\mathrm{d}\lambda}\bigg|_{\lambda=0} > 0 \,, \end{aligned} \tag{24}$$

resulting in

$$\sum_{i=1}^{N} \frac{\mathrm{d}\chi_i}{\mathrm{d}\lambda}\bigg|_{\lambda=0} > 0 \,. \tag{25}$$

The finer discretization of the lower span of the bar is responsible for the asymmetry of the curves shown in Fig. 7. (Mirror images of the discretizations of the bar, shown in Fig. 6, with respect to $x = L$, result in mirror images of the curves, shown in Fig. 7, with respect to $\lambda = 0$.) The strong mesh-dependence of the value of λ for which $\mathrm{d}(\det \mathbf{K}_T)/\mathrm{d}\lambda = 0$ proves that this value has no physical meaning. In general, it has nothing to do with the position of an extreme value of the stiffness of the structure.

$\mathrm{d}|P|/\mathrm{d}u_{ave} - \lambda$ diagram. $\mathrm{d}|P|/\mathrm{d}u_{\mathrm{ave}}$ represents the stiffness of the bar. Its determination requires knowledge of $u_{\mathrm{ave}}(\lambda)$. Fig. 8 shows the $u_{\mathrm{ave}} - \lambda$ diagram of the investigated bar. It was obtained with 256 Abaqus elements B22. Convergence studies with these elements and with Abaqus elements B21 have shown that u_{ave}, defined in (4) as the mean displacement, is an objective arc-length.

For the given example, the stiffness is always positive:

$$\frac{\mathrm{d}|P|}{\mathrm{d}u_{\mathrm{ave}}} = \frac{\frac{\mathrm{d}|P|}{\mathrm{d}\xi}}{\frac{\mathrm{d}u_{\mathrm{ave}}}{\mathrm{d}\xi}} = \frac{\frac{\mathrm{d}|P|}{\mathrm{d}|\lambda|}\frac{\mathrm{d}|\lambda|}{\mathrm{d}\xi}}{\frac{\mathrm{d}u_{\mathrm{ave}}}{\mathrm{d}\xi}} > 0 \,. \tag{26}$$

Substitution of

$$\frac{\mathrm{d}P}{\mathrm{d}\lambda} = \frac{\mathrm{d}|P|}{\mathrm{d}|\lambda|} = \bar{P} \tag{27}$$

and of

$$\frac{\mathrm{d}u_{ave}}{\mathrm{d}\xi} = \int \mathrm{d}s \,, \tag{28}$$

following from (3), into (27) yields

$$\frac{\mathrm{d}|P|}{\mathrm{d}u_{\mathrm{ave}}} = \frac{\bar{P}}{\int \mathrm{d}s}\frac{\mathrm{d}|\lambda|}{\mathrm{d}\xi} > 0 \quad \Rightarrow \quad \frac{\mathrm{d}|\lambda|}{\mathrm{d}\xi} > 0 \,. \tag{29}$$

Fig. 9 shows the stiffness of the bar as a function of λ.

Derivation of the stiffness of the bar with respect to $|\lambda|$ gives

$$\begin{aligned} \frac{\mathrm{d}}{\mathrm{d}|\lambda|}\left(\frac{\mathrm{d}|P|}{\mathrm{d}u_{\mathrm{ave}}}\right) &= \frac{\bar{P}}{\int \mathrm{d}s}\frac{\mathrm{d}}{\mathrm{d}|\lambda|}\left(\frac{\mathrm{d}|\lambda|}{\mathrm{d}\xi}\right) \\ &= \frac{\bar{P}}{\int \mathrm{d}s}\frac{\mathrm{d}}{\mathrm{d}\xi}\left(\frac{\mathrm{d}|\lambda|}{\mathrm{d}\xi}\right)\frac{\mathrm{d}\xi}{\mathrm{d}|\lambda|} = \frac{\bar{P}}{\int \mathrm{d}s}\frac{\frac{\mathrm{d}^2|\lambda|}{\mathrm{d}\xi^2}}{\frac{\mathrm{d}|\lambda|}{\mathrm{d}\xi}} \geq 0 \\ \Rightarrow \quad \frac{\mathrm{d}^2|\lambda|}{\mathrm{d}\xi^2} &\geq 0 \,, \end{aligned} \tag{30}$$

with the equality sign holding for $\lambda = 0$. Thus, the bar is stiffening for all $\lambda \neq 0$. Because of symmetry of the diagrams in Figs. 8 and 9 with respect to $\lambda = 0$, the second equation in (8) disintegrates into

$$\frac{\mathrm{d}\mathbf{K}_T}{\mathrm{d}\xi}(\lambda = 0) \cdot \frac{\mathrm{d}\mathbf{q}}{\mathrm{d}\xi}(\lambda = 0) = \mathbf{0} \,, \qquad \frac{\mathrm{d}^2\mathbf{q}}{\mathrm{d}\xi^2}(\lambda = 0) = \mathbf{0} \,. \tag{31}$$

In contrast to the minimum of $\mathrm{d}|P|/\mathrm{d}u_{\mathrm{ave}}$ at $\lambda = 0$, the $\det \mathbf{K}_T/\max(\det \mathbf{K}_T) - \lambda$ diagrams in Fig. 5, which are also symmetric with respect to $\lambda = 0$, have a maximum at $\lambda = 0$, incorrectly insinuating a maximum of the stiffness of a seemingly softening structure for all $\lambda \neq 0$. Accordingly, point M in Fig. 1(b) has nothing to do with a maximum of the stiffness of the torispherical pressure vessel head, see Fig. 1(a), subjected to internal pressure. In fact, the stiffness of the structure remains increasing also at the stability limit S^+, see Fig. 2. Hence, extreme values of $\det(K_T)$ have no physical meaning.

3.2. IPE400 bar subjected to an eccentric compressive force

3.2.1. Preliminaries

Fig. 10 shows the undeformed structure. The length of the IPE 400 bar, L, is equal to 5 m. The bar is simply supported at its two ends. Its cross-section is shown in Fig. 3(b). The values of A, E, and ν were given in the beginning of Section 3.1.1. The second moment of inertia, I_z, of the cross-section, is equal to $1.3198\ 10^{-5}\,\mathrm{m}^4$. Fig. 3(b) shows the deformed structure. It is quasi-statically loaded by an eccentric

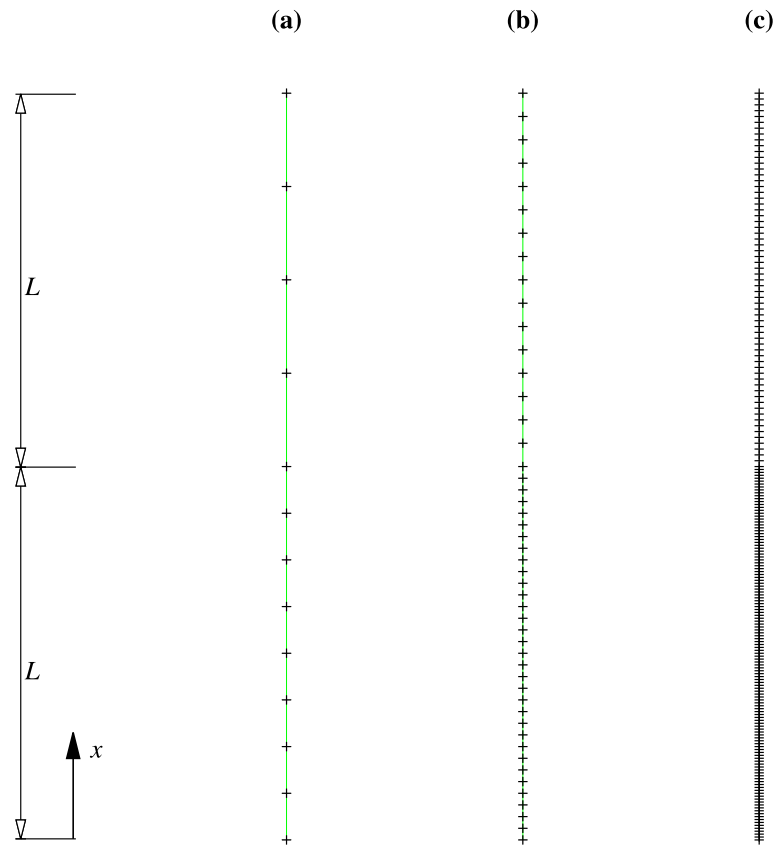

Fig. 6. Discretization of the bar shown in Fig. 3 with Abaqus elements B22: (a) 4 finite elements in the upper span and 8 in the lower span, (b) 16 and 32 elements, and (c) 64 and 128 elements.

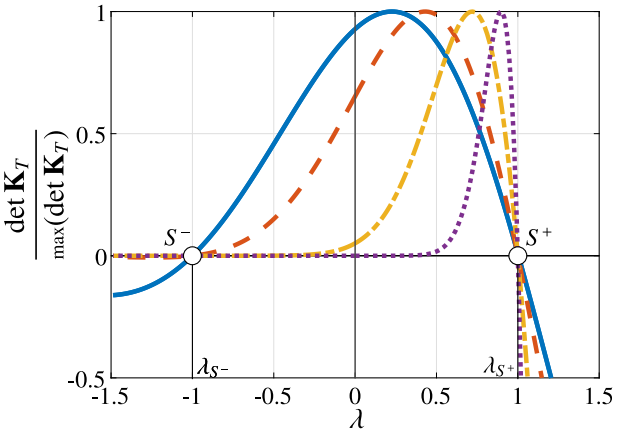

Fig. 7. $\det \mathbf{K}_T / \max(\det \mathbf{K}_T) - \lambda$ diagrams obtained with Abaqus elements B22 for the three discretizations shown in Fig. 6: (a) 4 and 8 elements (solid blue curve) (b) 16 and 32 elements (dotted red curve), (c) 64 and 128 elements (dash-dotted yellow curve) and, additionally, for 256 and 512 elements (dotted purple curve). (For interpretation of the references to color in this figure legend, the reader is referred to the web version of this article.)

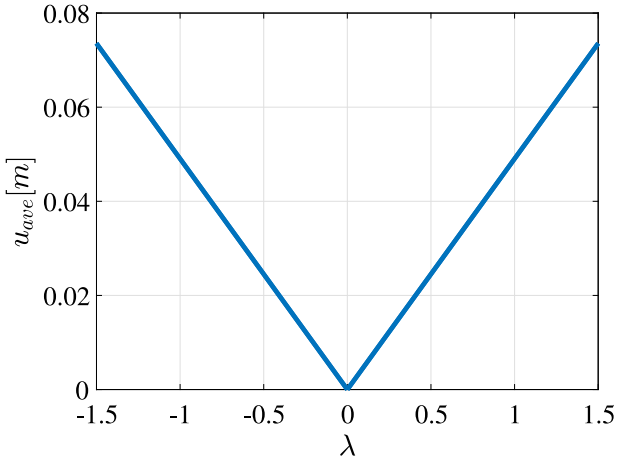

Fig. 8. $u_{ave} - \lambda$ diagram of the bar shown in Fig. 3.

compressive force $P = \lambda \bar{P}$, where $\bar{P}$ denotes the reference load, chosen as $1.1\ 10^6$ N, and λ stands for a dimensionless proportionality factor. The value of the eccentricity e of the load was chosen as 0.5 m. v denotes the displacement of the axis of the bar in the direction of the coordinate y.

The differential equation for the displacement curve of the bar is given as (Mang and Hofstetter, 2018; Pichler and Aminbaghai, 2020):

$$\frac{\frac{\mathrm{d}^2 v}{\mathrm{d}x^2}}{\left[1 + \left(\frac{\mathrm{d}v}{\mathrm{d}x}\right)^2\right]^{3/2}} + \alpha^2 v = -\alpha^2 e\,, \tag{32}$$

where

$$\alpha^2 = \frac{\lambda \bar{P}}{E I_z}\,. \tag{33}$$

Since (32) has no analytical solution, the problem was solved by the FEM. The numerical investigation was again carried out with the help of the commercial software Abaqus (Abaqus User Manual, 2020), using SI units, *i.e.* "m" and "kg/s^2". Details of the Abaqus elements B31,

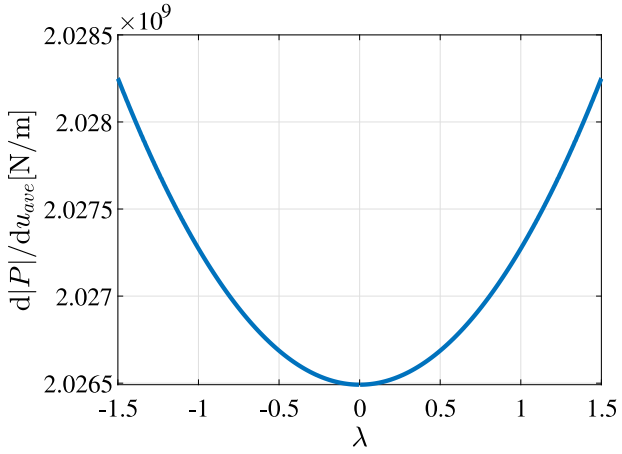

Fig. 9. $\mathrm{d}|P|/\mathrm{d}u_{ave} - \lambda$ diagram for the bar shown in Fig. 3.

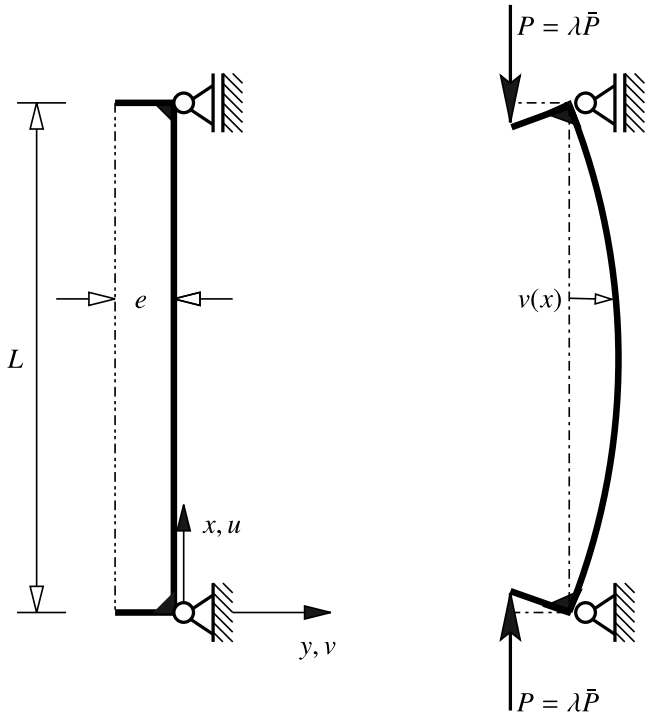

Fig. 10. Bar subjected to an eccentric compressive force, adapted from Mang and Hofstetter (2018): (a) undeformed structure, (b) deformed structure.

Table 2
Details of the Abaqus elements B31, B31OS, B32, B32OS, and B33 (Abaqus User Manual, 2020; Kalliauer et al., 2021), the hybrid Elements, ending with "H", are identical to the disp.-elements, except they do have additionally 3 d.o.f. for the two-noded linear elements and 6 addionally d.o.f. for the three noded and the cubic elements.

Designation	Formulation	# of nodes	# of d.o.f.
Abaqus B31	3D, displ., Timoshenko	2/linear	12(= 2 · 6)
Abaqus B31OS	3D, displ., Timoshenko, open section	2/linear	14(= 2 · 7)
Abaqus B32	3D, displ., Timoshenko	3/quad.	18(= 3 · 6)
Abaqus B32OS	3D, displ., Timoshenko, open section	3/quad.	21(= 3 · 7)
Abaqus B33	3D, displ., Bernoulli	2/cubic	12 + 6

B31OS, B32, B32OS, and B33 (Abaqus User Manual, 2020), employed in the analysis, are given in Table 2.

In order to check the mesh-dependence of the results, the bar was discretized with (a) five and (b) ten finite elements.

3.2.2. Numerical results

$\chi_1 - \lambda$ diagrams and det $\mathbf{K}_T$/det $(\mathbf{K}_T)_0 - \lambda$ diagrams. Fig. 11(a) and (b) show $\chi_1 - \lambda$ diagrams obtained with 5 and 10 finite elements, respectively.

A comparison of corresponding curves in Fig. 11(a) and (b) indicates the insensitivity of the function $\chi_1(\lambda)$ to the two discretizations of the bar. It is seen, however, that the eigenvalue curves obtained with the Euler–Bernoulli element deviate significantly from the ones obtained with the three Timoshenko elements. The rings on these curves mark minimum values of χ_1. They satisfy the condition

$$\mathbf{r}_1 \cdot \frac{\mathrm{d}\mathbf{K}_T}{\mathrm{d}\lambda} \cdot \mathbf{r}_1 = 0\,, \tag{34}$$

as follows from derivation of (11) with respect to λ (Mang and Jia, 2013; Mang et al., 2016; Aminbaghai and Mang, 2012). Fig. 11 shows that the function $\chi_1(\lambda)$ has no zero position inside the considered range of λ. This differs from the stability limit, $\lambda = 1$, obtained by means of second-order-theory, *i.e.* by omitting the term $(\mathrm{d}v/\mathrm{d}x)^2$ in the denominator of (32).

Fig. 12(a) and (b) show the $\det \mathbf{K}_T / \det(\mathbf{K}_T)_0 - \lambda$ diagrams obtained with 5 and 10 elements, respectively.

The rings on the curves in Fig. 12 mark minimum values of $\det \mathbf{K}_T$. It is seen that the curves depend on both the chosen finite element and the number of finite elements. According to Table 2, the four elements used in the numerical investigation of the present example have different numbers of d.o.f.. Consequently, the number of eigenvalues, N, will vary even if the number of finite elements remains unchanged. Hence,

$$\frac{\det \mathbf{K}_T}{\det(\mathbf{K}_T)_0} = \prod_{i=1}^{N} \chi_i \tag{35}$$

is not a mechanically objective quantity in the previously defined sense. Consequently, the positions of the extreme values of this quantity are mechanically meaningless, as was shown already in the first example. Although the initial decrease of $\det \mathbf{K}_T / \det(\mathbf{K}_T)_0$, see Fig. 12, correlates with the initial decrease of the stiffness of the bar, *i.e.* with its initial softening, the different positions of the first minimum values of this quantity and the existence of further extreme values of $\det \mathbf{K}_T / \det(\mathbf{K}_T)_0$ corroborate their mechanical irrelevance.

Load–displacement diagrams. Fig. 13(a) shows the $v_{\max} - \lambda$ diagram, where $v_{\max}$ denotes the largest transverse displacement of the bar. This curve has a point of inflection at $\lambda \approx 0.68$. Fig. 13(b) shows the $u_{\max} - \lambda$ diagram, where $u_{\max}$ stands for the largest axial displacement of the bar. This curve has a point of inflection at $\lambda \approx 0.93$. (The dependence of the functions $v_{\max}(\lambda)$ and $u_{\max}(\lambda)$ on the chosen finite element and on the number of finite elements considered in the numerical investigation is negligibly small, resulting in overlapping curves.) Because of

$$\lambda(v_{\max})\Big|_{\frac{\mathrm{d}^2 v_{\max}}{\mathrm{d}\lambda^2}=0} \neq \lambda(u_{\max})\Big|_{\frac{\mathrm{d}^2 u_{\max}}{\mathrm{d}\lambda^2}=0}\,, \tag{36}$$

the points of inflection of the two curves are merely local quantities, related to displacements of individual points.

Fig. 14(a) shows the $u_{\mathrm{ave}} - \lambda$ diagram of the bar. The curve has a point of inflection at $\lambda \approx 0.891$. It is seen that

$$\lambda(v_{\max})\Big|_{\frac{\mathrm{d}^2 v_{\max}}{\mathrm{d}\lambda^2}=0} < \lambda(u_{\mathrm{ave}})\Big|_{\frac{\mathrm{d}^2 u_{\mathrm{ave}}}{\mathrm{d}\lambda^2}=0} < \lambda(u_{\max})\Big|_{\frac{\mathrm{d}^2 u_{\max}}{\mathrm{d}\lambda^2}=0}\,. \tag{37}$$

In contrast to the two aforementioned local quantities, $\lambda(u_{\mathrm{ave}})\big|_{\frac{\mathrm{d}^2 u_{\mathrm{ave}}}{\mathrm{d}\lambda^2}=0}$ is a global quantity. It marks, in a mechanically objective manner, the transition from the initially softening structure to a stiffening structure.

Another possible global mechanical quantity is the variation of the work W done by the load. An infinitesimal increment of W is given as:

$$\mathrm{d}W = P\,\mathrm{d}s\,, \tag{38}$$

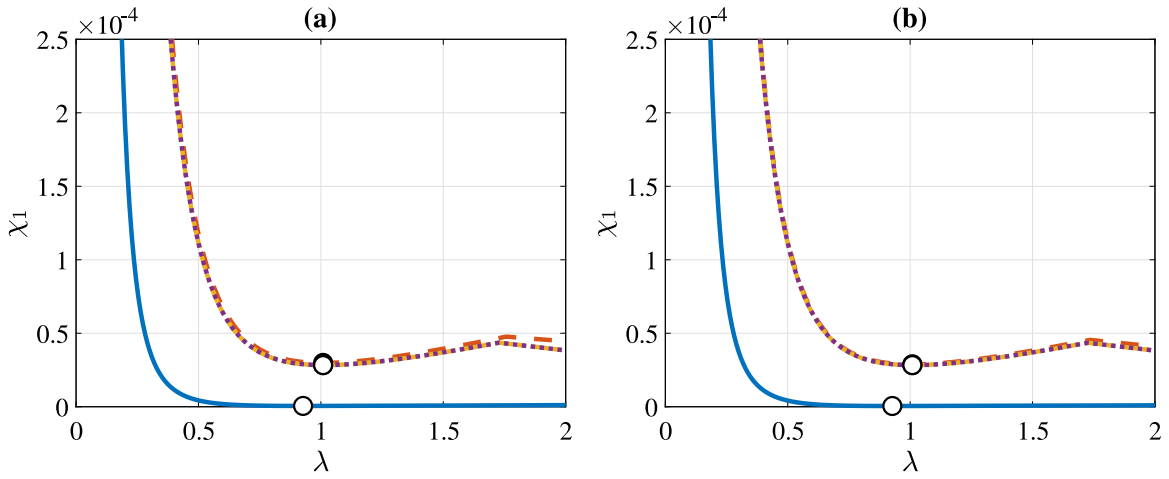

Fig. 11. Bar subjected to an eccentric compressive force: $\chi_1 - \lambda$ diagrams obtained with (a) 5 and (b) 10 Abaqus elements B33 (solid blue curves), B31OS (dashed red curves), B32 (dash-dotted yellow curves), and B32OS (dotted purple curves). (For interpretation of the references to color in this figure legend, the reader is referred to the web version of this article.)

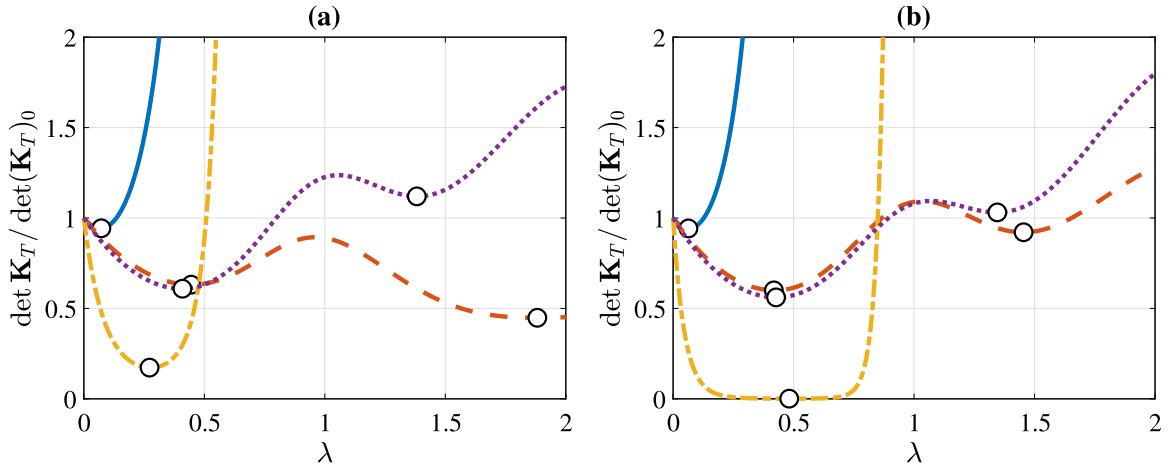

Fig. 12. Bar subjected to an eccentric compressive force: $\det \mathbf{K}_T / \det(\mathbf{K}_T)_0 - \lambda$ diagrams obtained with (a) 5 and (b) 10 Abaqus elements B33 (solid blue curves), B31OS (dashed red curves), B32 (dash-dotted yellow curves), and B32OS (dotted purple curves). (For interpretation of the references to color in this figure legend, the reader is referred to the web version of this article.)

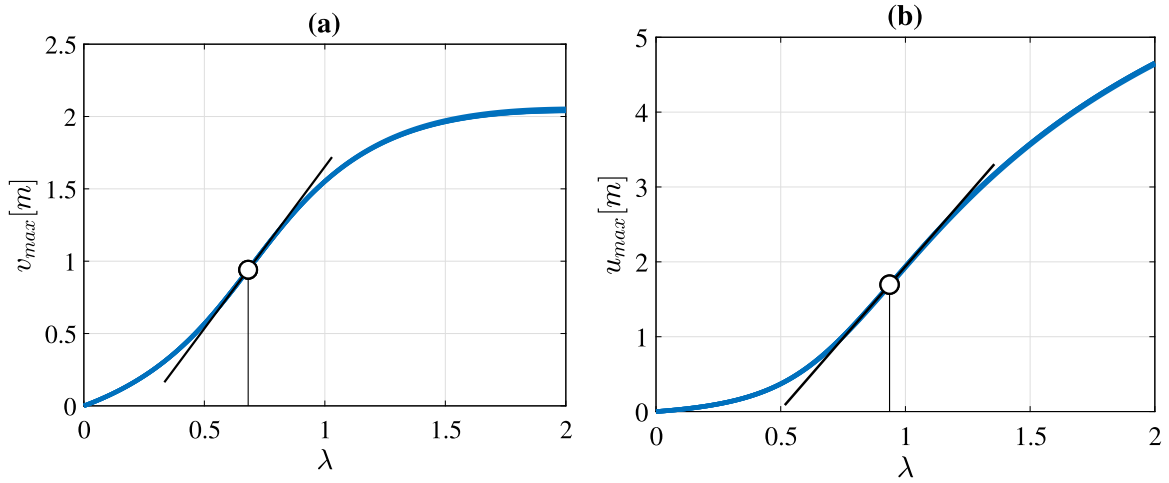

Fig. 13. Bar subjected to an eccentric compressive force: (a) $v_{\max} - \lambda$ diagram, (b) $u_{\max} - \lambda$ diagram.

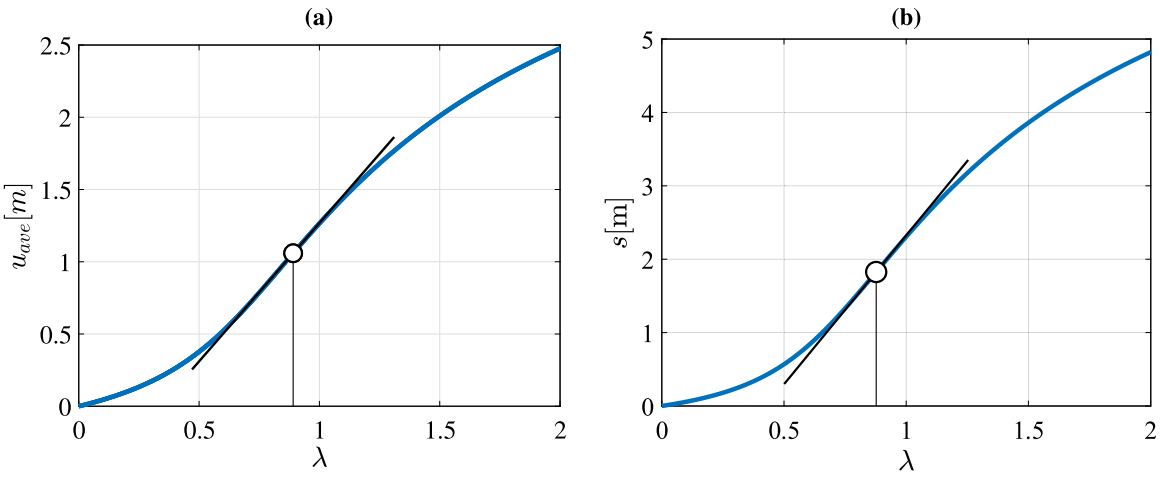

Fig. 14. Bar subjected to an eccentric compressive force: (a) $u_{ave} - \lambda$ diagram, (b) $s - \lambda$ diagram.

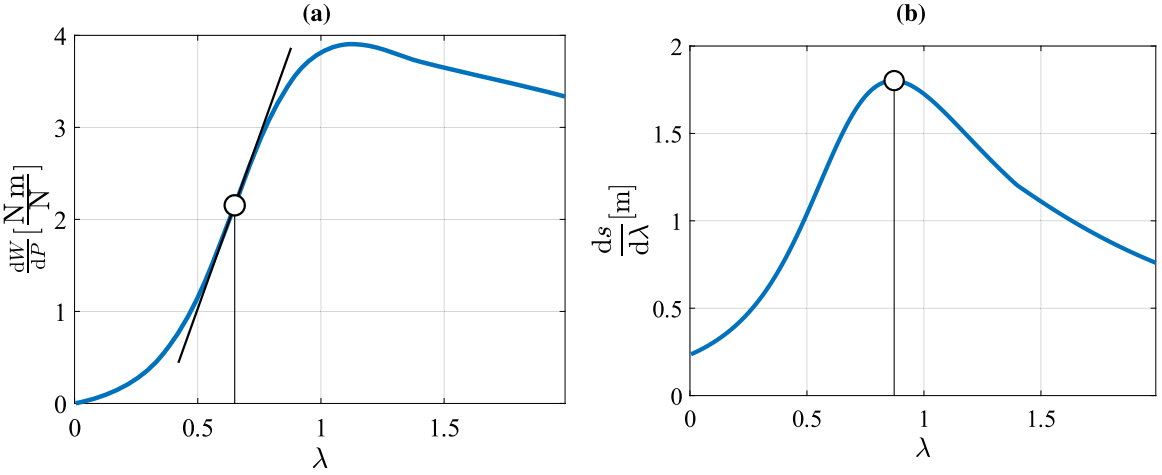

Fig. 15. Bar subjected to an eccentric compressive force: (a) $dW/dP - \lambda$ diagram, (b) $ds/d\lambda - \lambda$ diagram.

where ds denotes an infinitesimal increment of the movement of the point of loading. Thus,

$$\frac{dW}{dP} = \frac{dW}{ds} \cdot \frac{ds}{dP} = P \frac{ds}{dP} = \lambda \bar{P} \frac{ds}{\bar{P}\, d\lambda} = \lambda \frac{ds}{d\lambda} \tag{39}$$

with s as the difference of the movements of the two points of loading. Fig. 14(b) shows the $s - \lambda$ diagram of the bar. The curve has a point of inflection at $\lambda \approx 0.878$.

Fig. 15(a) shows the $dW/dP - \lambda$-diagram with a point of inflection at $\lambda \approx 0.65$. Fig. 15(b) illustrates the $ds/d\lambda - \lambda$ diagram, with a maximum at $\lambda \approx 0.87$.

3.2.3. Rates of convergence of u_{ave} for uniform and non-uniform meshes

The bar shown in Fig. 10 was used to study the rates of convergence of u_{ave} for uniform as well as non-uniform meshes of finite elements. The investigation was carried out for $\lambda = 1 \Rightarrow P = \bar{P} = 1.1\ 10^3$ N.

The rate of convergence of u_{ave} was tested at the stability limit according to second-order theory ($\lambda = 1 \Leftrightarrow P = \bar{P} = 1.1\ 10^6$ N), where $\bar{P}$ denotes the buckling load according to this theory which disregards the term $(dv/dx)^2$ in the denominator of (32) (Kurrer, 2016). (Second-order theory is restricted to moderately large displacements.) Abaqus, which was used for the numerical investigation, however accounts for this term, which allows load intensities P larger than $\bar{P}$. Fig. 16 shows the undeformed and the deformed bar. For a bar discretized with at least 20 elements, independent of the chosen element, the value of the transverse displacement in the middle of the beam, v_{max}, is equal to 1.552 m.

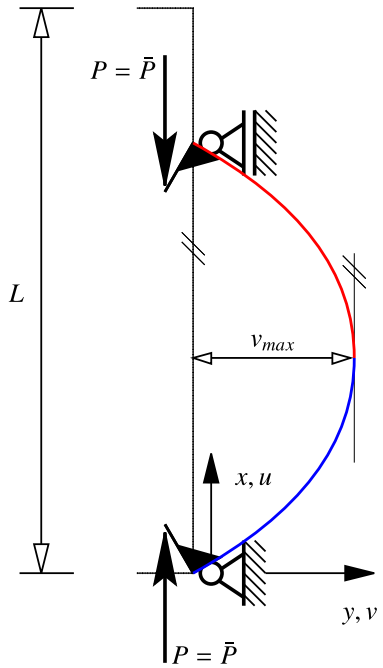

Fig. 16. Bar subjected to an eccentric compressive force $P = \bar{P} = 1.1\ t10^6$ N: Undeformed and deformed configuration.

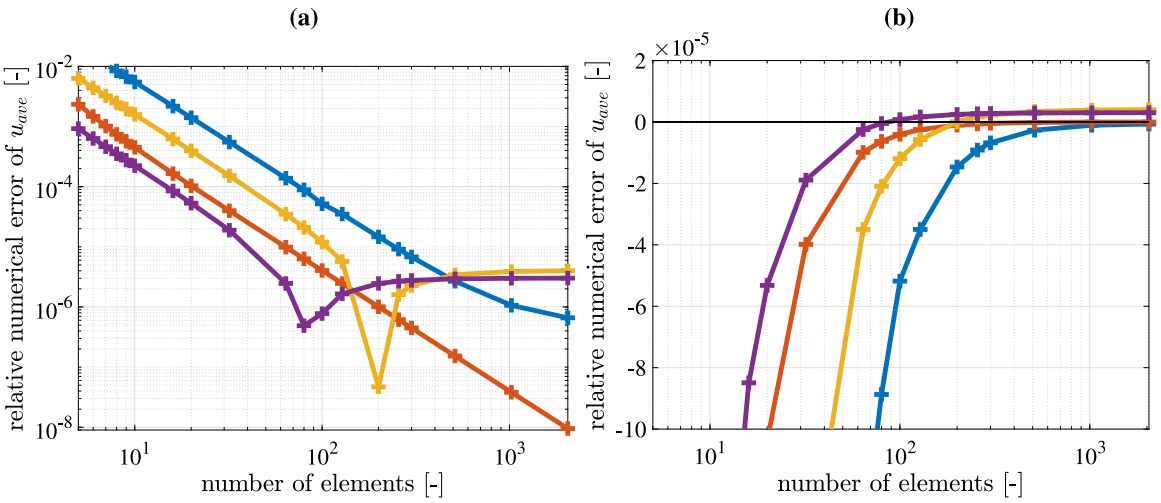

Fig. 17. Relative error of u_{ave}, computed with elements B31OSH (blue: uniform mesh, yellow: non-uniform mesh) and B32OSH (red: uniform mesh, purple: non-uniform mesh), respectively, shown on (a) a double-logarithmic and (b) a semi-logarithmic scale. (For interpretation of the references to color in this figure legend, the reader is referred to the web version of this article.)

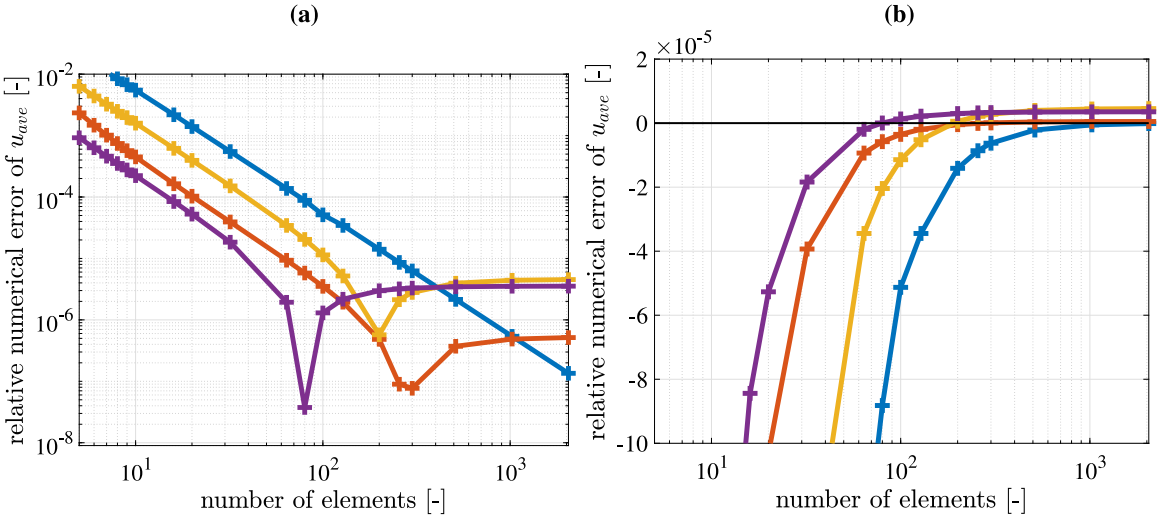

Fig. 18. Relative error of $u_{ave,B31}$ and of the Abaqus-result for u_{ave}, computed with elements B31OSH (blue: uniform mesh, yellow: non-uniform mesh) and B32OSH (red: uniform mesh, purple: non-uniform mesh), respectively, shown on (a) a double-logarithmic and (b) a semi-logarithmic scale. (For interpretation of the references to color in this figure legend, the reader is referred to the web version of this article.)

The number of elements for uniform meshes is ranging from 5 to 2048. For non-uniform meshes, the upper half of the bar, shown in red color, is discretized with 64 elements of equal length. The number of elements of equal length in the lower half of the bar, shown in blue color, is ranging from 5 to 2048. Details of the Abaqus elements in the numerical investigation are given in Table 2.

For all elements, the rates of convergence of u_{ave} are quadratic. Thus, dividing each element of a uniform mesh into two equally long elements, the previous numerical error is divided by a factor of 4 ± 0.002. Because of the small scatter of this factor of less than 1‰, the numerical error can be predicted to three significant digits before starting the calculation.

Fig. 17 refers to the relative error of u_{ave}, computed with elements B31OSH and B32OSH, for uniform as well as non-uniform meshes. The reference value to which the absolute error of u_{ave} is related will be introduced later.

At first, the results obtained with uniform meshes will be interpreted. The finest B32OSH-mesh consists of 2048 elements. It resulted in $u_{ave,B32-2048} = 1.275\,869\,613\,045$ m. The predicted error based on the trend in previous calculations with B32OSH, is equal to $-0.000\,000\,012\,135$ m. Consideration of this error yields $u_{ave,B32} = 1.275\,869\,625\,18$ m.

The finest B31OSH-mesh also consists of 2048 elements. It resulted in $u_{ave,B31-2048} = 1.275\,868\,783$ m. The predicted error, based on the trend of previous calculations with B31OSH, is equal to $-0.000\,000\,172$ m. Consideration of this error yields $u_{ave,B31} = 1.275\,868\,955$ m. Choosing this value as a reference value would result in a straight blue line in Fig. 17(a).

Since both meshes result in quadratic convergence (*i.e.* both have the same slope in Fig. 17(a)), the mesh with the smaller numerical error (*i.e.* the lower one of the two parallel lines in Fig. 17(a)) was chosen as the reference value, *i.e.* $u_{ave,ref} = u_{ave,B32}$, resulting in the straight red line in Fig. 17(a). The relative numerical difference, between $u_{ave,B31}$ and $u_{ave,B32}$ is $5.2\ 10^{-7}$. Because of this difference, the red curve in Fig. 17(a) is straight, which is not the case with the red curve in Fig. 18(a). Conversely, the blue curve in Fig. 18(a) is straight, which is not the case with the blue curve in Fig. 17(a). In Fig. 17, $u_{ave,B32}$ is the reference value, whereas in Fig. 17 it is $u_{ave,B31}$.

The value of the numerical error of u_{ave}, related to this reference value, is shown in Fig. 17. The difference between the result obtained

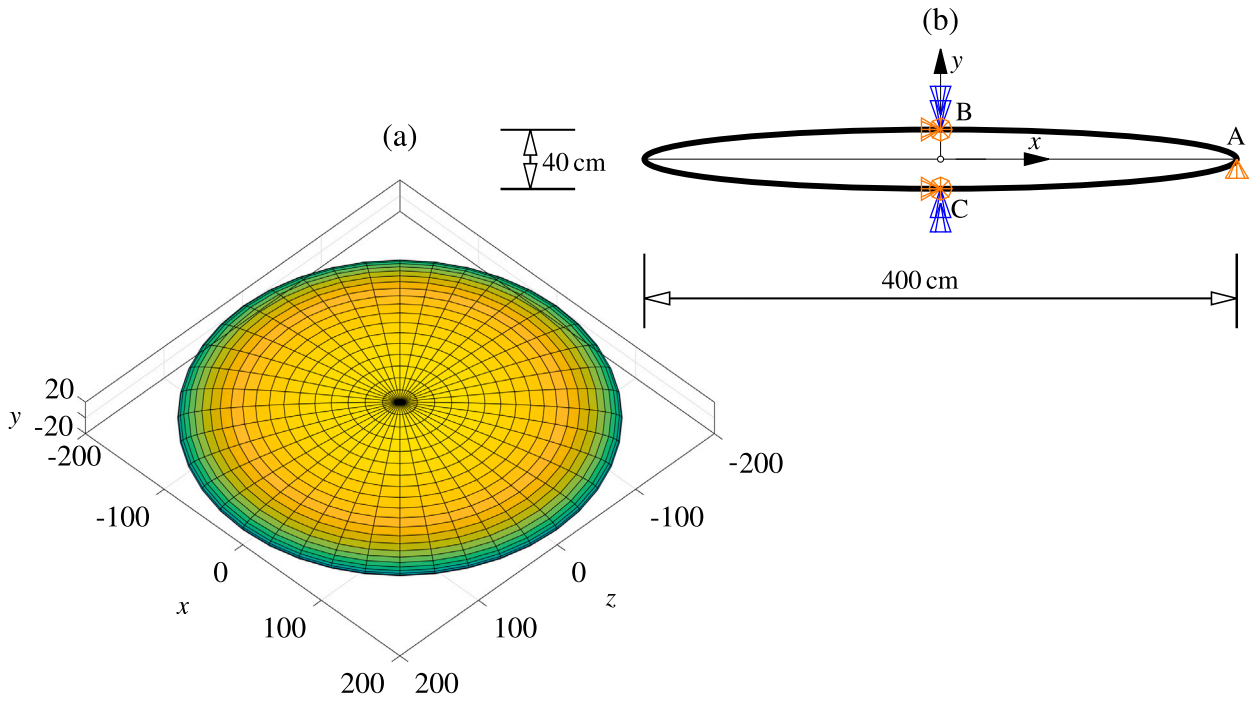

Fig. 19. Oblate rotational ellipsoidal shell subjected to internal pressure: (a) isometric view of the structure, (b) cross-section of the x–y-plane, boundary conditions: (α) ⚠: no translation in the y-direction, (β) ❄: no translation in the z-direction, (γ) ▷: no translation in the x-direction, (δ) ▲▼: no rotations around the y-axis.

with the finest mesh, consisting of 2048 B32OSH-elements, and the reference value, divided by u_{ave}, is 9.5 10^{-9}. It represents the right end of the red line in Fig. 17. The corresponding value, computed with the finest B31OSH-mesh, i.e. the one at the right end of the blue line, is larger, namely 6.6 10^{-7}. For the meshes with B31, B31H, B31OS and B32, B32H, B32OS elements, the same results were obtained as for the B31OSH-meshes and the B32OSH-meshes.

In the following, the results obtained with non-uniform meshes will be interpreted. The yellow and the purple curve in Fig. 17(a) refer to results for the relative numerical error of u_{ave}, obtained with different non-uniform B31OSH-meshes and B32OSH-meshes, respectively, of the previously described form. In case of the B31OSH-meshes, the sign of the numerical error changes at around 200 elements. For the B32OSH-meshes, such a change occurs between 80 and 100 elements. Fig. 17(b) elucidates that these sign changes represent transitions from underestimating to overestimating u_{ave}. The yellow and the purple curve in Fig. 17 have a relative numerical error of 4 10^{-6} and 3 10^{-6}, respectively, for the finest discretization of the lower half of the bar, consisting of 2048 elements, while the discretization of the upper half has been kept constant with 64 elements. This proves that u_{ave} converges also for local mesh-refinements of non-uniform meshes. However it is usually the coarsest subregion of the mesh that defines the order of the numerical error of a characteristic mechanical quantity. Consistent mesh-refinements of non-uniform meshes would converge to a much smaller numerical error.

A relative numerical error of less than 1%, which is the upper limit in Fig. 17(a), is generally insignificant. It was used in this subsection merely to demonstrate the rates of convergence of u_{ave} for different meshes.

3.3. Buckling of a stiffening structure of the form of an oblate rotational ellipsoidal shell subjected to internal pressure

3.3.1. Preliminaries

Fig. 19(a) contains an isometric view of the structure. Fig. 19(b) shows the cross-section in the x–y plane. The radius of the equator is 200 cm and the distance between the poles is 40 cm. The thickness of the shell is 0.5 cm. The modulus of elasticity, E, and Poisson's ratio, ν, are equal to 2.1 10^{11} kN/m^2 and 0.3, respectively. The reference pressure is chosen as 10^3 N/m^2. Fig. 19(b) also contains information about the boundary conditions. Point A is prevented from moving in the vertical direction. Points B and C are prevented from moving horizontally. Moreover, the shell is prevented from rotating around the y-axis. These boundary conditions would result in a statically determinate model if one half of the structure was considered. However, in the analysis the whole structure was taken into account. Hence, the model is statically indeterminate to the first degree.

Table 3
Details of the Abaqus elements S3 and S4 (Abaqus User Manual, 2020).

Designation	Formulation	# of nodes	# of d.o.f.
Abaqus S3	3D, displ.	3/linear	18 (= 3 · 6)
Abaqus S4R	3D, displ., reduced integration, hourglass control	4/linear	24 (= 4 · 6)

The problem was solved by the FEM. The numerical investigation was again carried out with the help of the commercial software Abaqus (Abaqus User Manual, 2020). Details of the Abaqus elements S3 and S4R, employed in the analysis, are given in Table 3.

The mesh consists of 42 675 elements.

3.4. Numerical results

The red curve in Fig. 20(a) shows the prebuckling branch of the λ–u_{ave} diagram of the perfect structure subjected to internal pressure. It stretches from the start of loading to the stability limit, denoted as S. A characteristic feature of this curve is its positive curvature. It shows that the shell is stiffening. However, this does not prevent it from buckling.

At first sight, Fig. 20(a) might be misleading. It gives the impression that point I is the stability limit and that the initial part of the postbuckling branch, *i.e.* the blue curve, signals stable equilibrium. Fig. 20(b) clarifies the situation. It explains that point I represents the snap-back point at the end of the unstable initial part of the post-buckling branch, shown as a dotted green curve. It starts at the true stability limit,

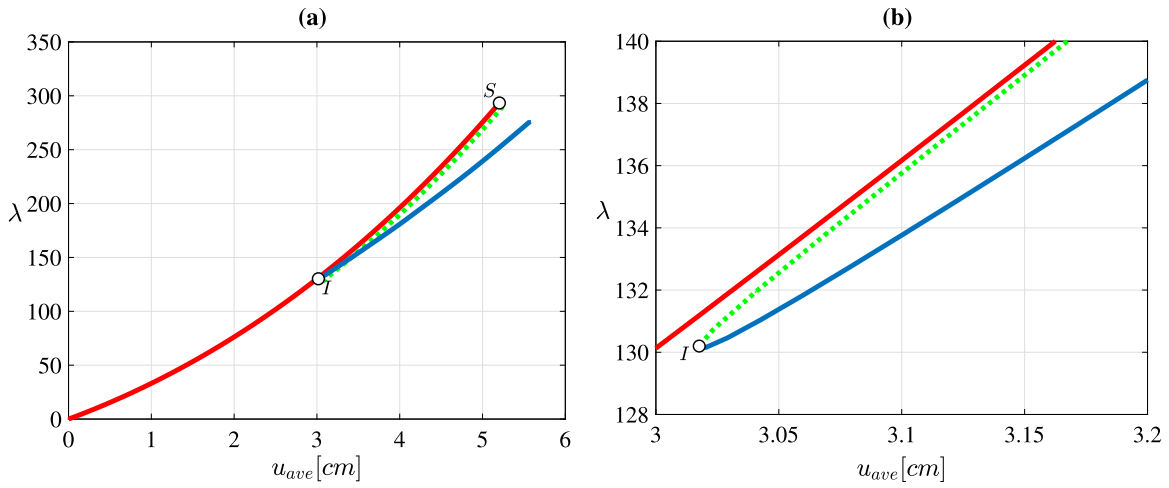

Fig. 20. Oblate rotational ellipsoidal shell: (a) prebuckling branch and initial part of the postbuckling branch of the perfect shell, (b) detail of (a). The green dotted curve in (a) has an offset of one linewidth to avoid overlapping with the red curve. (For interpretation of the references to color in this figure legend, the reader is referred to the web version of this article.)

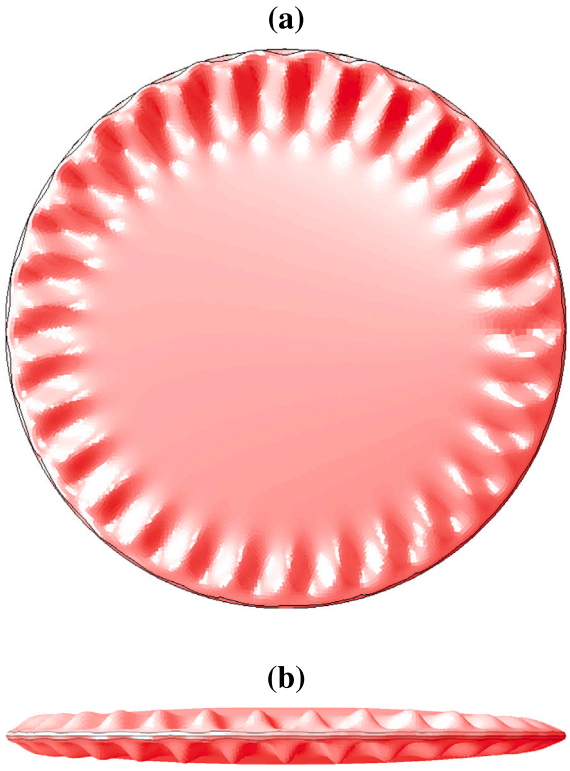

Fig. 21. Oblate rotational ellipsoidal shell subjected to internal pressure: (a) top view of the buckling mode, (b) front view of the buckling mode.

S. Hence, a stiffening structure is no safeguard against a potentially dangerous post-buckling behavior. An argument for relating λ to the global quantity u_{ave} rather than to a particular degree of freedom is the global character of loss of stability of the structure.

Fig. 21(a) shows a top view of the buckling mode of the shell. The number of buckling waves in the circumferential direction is 30. Fig. 21(b) shows a front view of the buckling mode of the structure.

4. Conclusions

- It was shown that $\mathrm{d}(\det \mathbf{K}_T)/\mathrm{d}\lambda = 0$ is not objective and therefore does not mark an extreme value of the stiffness of a loaded structure. Hence, it has nothing to do with the transition of a proportionally loaded stiffening structure to a softening structure or *vice versa*.
- The reason for the mechanical irrelevance of the sign of $\mathrm{d}(\det \mathbf{K}_T)/\mathrm{d}\lambda$ is the dependence of $\det \mathbf{K}_T$ on the product of the eigenvalues of a linear eigenvalue problem with $\mathbf{K}_T$ as one of the two coefficient matrices. The number of these eigenvalues, N, is equal to the number of d.o.f. of the FE model of the structure. Thus, it depends on both the number of d.o.f. of the chosen finite element and the number of finite elements. Hence, apart from $\det \mathbf{K}_T = 0$, $\det \mathbf{K}_T$ and, consequently, $\mathrm{d}(\det \mathbf{K}_T)/\mathrm{d}\lambda$ are no mechanically objective quantities.
- To underscore the argument concerning the mechanical irrelevance of $\mathrm{d}(\det \mathbf{K}_T)/\mathrm{d}\lambda = 0$ as a quantity that signals the transition from stiffening (softening) to softening (stiffening), the maximum values of the $\det \mathbf{K}_T / \det(\mathbf{K}_T)_0$ - λ diagrams in Figs. 5 and 7 were shown to correspond to a strictly stiffening structure. Irrespective of the direction of the applied load, the stiffness of the structure is increasing, albeit very little, with growing load intensity.
- The decrease of $\det \mathbf{K}_T(\lambda)$ before reaching the stability limit seems, at first glance, to support the widespread misconception that buckling of structures is necessarily preceded by a decrease of their stiffnesses.
- An oblate rotational ellipsoidal shell, subjected to internal pressure, was used as an example for buckling of a stiffening shell. It was illustrated that a stiffening structure is no safeguard against a potentially dangerous post-buckling behavior.
- It was shown that the conventional definition of stiffening (softening) structures at a specific load level as $\mathrm{d}^2\lambda/(\mathrm{d}q_i)^2 > 0$ (< 0), where q_i denotes a characteristic d.o.f., is lacking mechanical objectivity. This was done by means of a mechanically objective dimensionless arc-length ξ. In particular, it was demonstrated that the value of λ, for which $\mathrm{d}^2\lambda/\mathrm{d}\xi^2 = 0$, marking the transition from an initially softening to a stiffening bar subjected to eccentric compression, correlates, on the one hand, with $\mathrm{d}^2\lambda/\mathrm{d}q_i^2 > 0$ and, on the other hand, with $\mathrm{d}^2\lambda/\mathrm{d}q_j^2 < 0$, where both q_i and q_j denote a characteristic d.o.f. .

Based on these conclusions, the answer to the question posed in the title of this paper is conditionally affirmative. For the mechanically objective arc-length ξ, defined in this work, $\mathrm{d}^2\lambda/(\mathrm{d}\xi)^2 > 0$ (< 0), assuming $\mathrm{d}\lambda/\mathrm{d}\xi > 0$, with $\lambda > 0$, $\xi > 0$, are mechanically unambiguous definitions of stiffening and softening structures.

CRediT authorship contribution statement

Johannes Kalliauer: Methodology, Software, Validation, Formal analysis, Numerical investigation, Data curation, Writing – review & editing, Visualization. **Herbert A. Mang:** Conceptualization, Validation, Formal analysis, Writing – original draft, Writing – review & editing, Project administration, Funding acquisition, Supervision.

Declaration of competing interest

The authors declare that they have no known competing financial interests or personal relationships that could have appeared to influence the work reported in this paper: The financial support was provided by Austrian Science Fund, an organization financed by the Austrian Federal Government, who is interested in funding Austrian non-profit oriented unbiased scientific research, with an international scientific impact. This funding does not need to be disclosed according to https://declarations.elsevier.com/homeElsevier's Declaration Tool, since it is a government agency.

Acknowledgments

This work is supported by the *Austrian Science Fund (FWF)* under Grant *P 31617-N32 [Pseudo-kinematic invariants - gems in FE structural analyses]*.

Appendix. List of symbols

Variable	Unit	Explanation
e	[m]	Eccentricity of the normal force
$\mathbf{q}$	[m; rad]	Vector of nodal degrees of freedom in the framework of the FEM, introduced in (1)
$\mathbf{q}_i, \mathbf{q}_j$	[m; rad]	Vectors of nodal degrees of freedom of points i and j in the framework of the FEM
$\mathbf{r}_i$	[m; rad]	ith orthonormal eigenvector of the eigenvalue-problem (11)
s	[m]	Axial coordinate, introduced in Eq. (3)
$\mathbf{u}$	[m]	Displacement vector of an arbitrary point
u_{ave}	[m]	Average displacement, defined in (4)
$u_{\text{ave,B31}}$	[m]	Average displacement, derived with linear Timoshenko-elements
$u_{\text{ave,B32}}$	[m]	Average displacement, derived with quadratic Timoshenko-elements
u	[m]	Displacement component in the x-direction
v	[m]	Displacement component in the y-direction
w	[m]	Displacement component in the z-direction
A	[m^2]	Area of the cross-section of a bar
E	[N/m^2]	Modulus of elasticity
$\mathbf{I}$	[1]	Identity matrix, introduced in (12)
I_y	[m^4]	Relevant principal second moment of area, around the strong axis, of the cross-section of a bar
I_y	[m^4]	Relevant principal second moment of area, around the weak axis, of the cross-section of a bar
$\mathbf{K}_T$	$\left[\frac{N}{m}; \frac{N\,m}{rad}; N\right]$	Tangent stiffness matrix, introduced in (11)
$(\mathbf{K}_T)_0$	$\left[\frac{N}{m}; \frac{N\,m}{rad}; N\right]$	Tangent stiffness matrix at the onset of proportional loading, introduced in (11)
L	[m]	Length of a bar
N	[1]	Number of active degrees of freedom in the FEM-simulations, introduced in (11)
P	[N]	Node force, defined in (26).
$\bar{P}$	[N]	Reference node force, defined in (27).
$\bar{\mathbf{P}}$	[N; N m]	Vector of reference work-equivalent node forces, introduced in (1) as $\bar{\mathbf{P}} = \mathbf{P}/\lambda$.
λ	[1]	Proportionality factor of the load intensity
λ_S	[1]	Value of λ at the stability limit
ξ	[m]	Arc length of the FEM-displacements, defined in (3)
χ_i	[1]	ith eigenvalue in (11)

References

Abaqus User Manual, 2020. Abaqus 2021 theory guide.

Adachi, J., Benicek, M., 1964. Buckling of torispherical shells under internal pressure. Exp. Mech. 4 (8), 217–222. http://dx.doi.org/10.1007/BF02322954.

Aminbaghai, M., Mang, H.A., 2012. Characteristics of the solution of the consistently linearized eigenproblem for lateral torsional buckling. Bull. Georgian Natl. Acad. Sci. 6 (1), 47–58.

Bourbaki, N., 1998. Algebra I: Chapters 1-3, Vol. 1, first ed. Springer Science & Business Media.

Denman, E.D., Beavers, Jr., A.N., 1976. The matrix sign function and computations in systems. Appl. Math. Comput. 2 (1), 63–94. http://dx.doi.org/10.1016/0096-3003(76)90020-5.

Forrester, P.J., 2018. Meet andréief, bordeaux 1886, and andreev, kharkov 1882-83. pp. 1–9, arXiv preprint arXiv:1806.10411.

Galletly, G.D., 1982. The buckling of fabricated torispherical shells under internal pressure. In: Ramm, E. (Ed.), Buckling of Shells. Springer, pp. 429–466. http://dx.doi.org/10.1007/978-3-642-49334-8_15.

Helnwein, P., 1996. Zur initialen Abschätzbarkeit von Stabilitätsgrenzen auf nichtlinearen Last-Verschiebungspfaden elastischer Strukturen mittels der Methode der Finiten Elemente [in German: On *ab initio* accessability of stability limits on nonlinear load-displacment paths of elastic structures by means of the finite element method]. (Ph.D. thesis). Vienna University of Technology [now TU Wien], Vienna, Austria, URL https://permalink.catalogplus.tuwien.at/AC02254015.

Helnwein, P., Mang, H.A., 1997. An asymptotic approach for the evaluation of errors resulting from estimations of stability limits in nonlinear elasticity. Acta Mech. 125 (1), 235–254. http://dx.doi.org/10.1007/BF01177311.

Kalliauer, J., Malendowski, M., Mang, H.A., 2021. On a remarkable geometric-mechanical synergism based on a novel linear eigenvalue problem. Acta Mech. 232 (12), 4969–4985. http://dx.doi.org/10.1007/s00707-021-03091-5.

Kanodia, V.L., Gallagher, R.H., Mang, H.A., 1977. Instability analysis of torispherical pressure vessel heads with triangular thin-shell finite elements. J. Press. Vessel Technol. 99 (1), 64–74. http://dx.doi.org/10.1115/1.3454521.

Kenney, C.S., Laub, A.J., 1995. The matrix sign function. IEEE Trans. Automat. Control 40 (8), 1330–1348. http://dx.doi.org/10.1109/9.402226.

Kim, B.-S., Song, J.-K., 2016. Seismic responses of seismically isolated nuclear power plant structure considering post-yield stiffness of EQS bearing. J. Earthq. Eng. Soc. Korea 20 (5), 319–329. http://dx.doi.org/10.5000/EESK.2016.20.5.319.

Kurrer, K.-E., 2016. Die ersten technikwissenschaftlichen Grundlagendisziplinen: Baustatik und Technische Mechanik. In: Geschichte der Baustatik. John Wiley & Sons, Ltd, Berlin, pp. 114–121. http://dx.doi.org/10.1002/9783433606438.ch3, Ch. 3.

Mang, H.A., 2017. Evolution and verification of a kinematic hypothesis for splitting of the strain energy. Comput. Methods Appl. Mech. Engrg. 324, 74–109. http://dx.doi.org/10.1016/j.cma.2017.05.028.

Mang, H.A., Hofstetter, G., 2018. Festigkeitslehre [in German: Strength of Materials], fifth ed. Springer Vieweg, Berlin, Heidelberg, http://dx.doi.org/10.1007/978-3-662-57564-2.

Mang, H.A., Jia, X., 2013. Mathematical conditions for and physical meaning of a maximum of the determinant of $\mathbf{K}_T$ in the prebuckling regime. Adv. Eng. Softw. 62–63, 3–8. http://dx.doi.org/10.1016/j.advengsoft.2013.04.023.

Mang, H.A., Pavlicek, S., Jia, X., 2016. The buckling sphere: A symbiosis of mechanics and geometry. Comput. Methods Appl. Mech. Engrg. 309, 325–363. http://dx.doi.org/10.1016/j.cma.2016.05.033.

Mehta, M.L., 2004. Hermitian matrices coupled in a chain. In: Random Matrices, Pure and Applied Mathematics, vol. 142, third ed. Academic Press, pp. 444–445. http://dx.doi.org/10.1016/S0079-8169(04)80113-2.

Pichler, B.L.A., Aminbaghai, M., 2020. 202.068 Baustatik 2 [in German: 202.068 Structural Analysis - Static 2]. Tech. rep., TU Wien, Vienna, Austria, URL https://tiss.tuwien.ac.at/course/courseDetails.xhtml?courseNr=202068.

Wang, T., Zhou, H., Zhang, X., Ran, T., 2018. Stability of an explicit time-integration algorithm for hybrid tests, considering stiffness hardening behavior. Earthq. Eng. Eng. Vib. 17 (3), 595–606. http://dx.doi.org/10.1007/s11803-018-0465-6.